Assessment of interface failure behaviour for brittle adhesive using the three-point bending test

Thiago Birro, Maëlenn Aufray, Eric Paroissien, Frédéric Lachaud

Assessment of interface failure behaviour for brittle adhesive using the three-point bending test

Thiago V. Birro [a,b], Maëlenn Aufray [b,*], Eric Paroissien [a], Fréderic Lachaud [a]

[a] Institut Clément Ader (ICA), Université de Toulouse, ISAE-SUPAERO, INSA, IMT MINES ALBI, UTIII, CNRS, 3 Rue Caroline Aigle, 31400, Toulouse, France
[b] CIRIMAT, Université de Toulouse, CNRS, INPT, UPS, 4, allée Émile Monso -BP 44362, 31030, Toulouse Cedex 4, France

ARTICLE INFO

Adhesive failure
Three-point bending test
Coupled criterion
Macro-element
Interfacial properties

ABSTRACT

In the framework of the adhesive bonding, the assessment of interfacial properties has an essential role in determining the adhesive joints' global responses. Various surface preparations are available for each type of metallic substrate. There are plenty of tests widely used for mechanical characterisation to determine the adhesive properties and few tests to assess interfacial properties. For such a case, a specific three-point bending test can be applied to examine the interactions between adhesive and substrate. On the other hand, a direct comparison of the critical force is not always possible because of geometrical incompatibility. A practical solution for the last issue is applying a coupled stress-energy criterion (CC) since the interface properties are independent of the substrate thickness. Hence, CC and the macro-element technique were applied to determine the interfacial properties using an aluminium alloy 2024-T3 as substrate and the adhesive DGEBA/DETA™ under many preparation conditions.

As a result, the three-point bending test's overall behaviour was established in terms of interface strength (*adherence*), including incremental energy release rate and critical stress. Thus, this paper can be read as the first work towards the ability to predict the interface failure in the frame of three-point bending test using different geometries. In conclusion, the occurrence of an adhesive or cohesive failure and the unstable or a stable failure propagation of the bonded joints were sorted and classified as a function of interface properties.

1. Introduction

Adhesive bonding technologies have been used in an ever-growing number of areas as diverse as automotive, aeronautic, microelectronics, naval, biomedical, etc. Different sectors pursue cost-effective structures and the increasing of the strength-to-mass structural ratio. Bonded assemblies present other interesting benefits, such as an improvement in both fatigue strength and static strength stiffness, a continuous and more uniform load transfer, and high damping properties [1,2]. However, specific needs have to comply with each industrial sector, such as understanding the factors that affect the adhering systems (coating-substrate or adhesive-substrate system) [3,4].

To avoid any eventual misunderstanding, the meaning in this paper of terms adherence and adhesion are provided hereafter: *Adherence* is applied to quantify the strength at the interface between an adhesive and a substrate for adherence test geometry – it can be defined as a force, stress, energy, etc. Nevertheless, the term *Adhesion* comprises the fundamental intermolecular force or bonds acting across a bi-material media interface.

The most widely mechanical tests used for bonded assemblies (single-lap joint, double cantilever beam) are a classical sandwich substrate/adhesive/substrate assembly configuration, consisting of two identical interfaces (see Fig. 1-a). Most of these tests were conceived to promote a failure within the adhesive layer (cohesive failure). In the frame of an interface debonding, Legendre et al. (2018) [5] proposed a modified Arcan test, in which a steel blade was introduced into the adhesive layer (substrate/adhesive/blade/adhesive/substrate). The steel blades were prepared with different surface treatments (ST) and solicited under shear loading. Each ST presented a specific fracture response: interface debonding or cohesive failure. Finally, the interfacial properties were computed via Finite Element (FE) method, based on the experimental results. Zebar et al. (2020) [6] determined the interfacial properties using a closed-form solution and FE method, established on pre-cracked interfaces of four-point bending specimens, comprising a single interface (see Fig. 1-b).

Roche et al. (1982) [7] also proposed a specific three-point bending test (3PBT) - ISO 14679-1997 [8] to assess interfacial debonding. The specimen comprises a substrate/adhesive or substrate/coating/adhesive

* Corresponding author.
E-mail address: maelenn.aufray@ensiacet.fr (M. Aufray).

https://doi.org/10.1016/j.ijadhadh.2021.102891.

Nomenclature and units

a	crack length (mm)
a_c	critical crack length (mm)
A_j	extensional stiffness (N) of adherend j
b_a	adhesive width (mm)
b_{over}	overlap width (mm)
b_s	substrate width (mm)
D	the displacement (mm) of central roller
D_c	critical displacement (mm) in three-point bending test
D_j	the bending stiffness (N.mm^2) in adherend j
e_{rem}	reminder adhesive layer (μm) on the adherend
F_c	critical force (N) in the three-point bending test
h_a	the thickness (mm) of adhesive layer
h_j	the thickness (mm) of adherend j
h_s	the thickness (mm) of the substrate
H_j	the shear stiffness (N.mm^2) of the adherend j
k_I	interfacial stiffness (MPa/mm) under mode I
k_{II}	interfacial stiffness (MPa/mm) under mode II
K_{spec}	the overall stiffness of the specimen (N/mm)
k_{subst}	the overall stiffness of the substrate (N/mm)
L	length (mm) of bonded overlap
M_j	bending moment (N.mm) in adherend j about the z-direction
N_j	normal force (N) in adherend j in the x-direction
R^2	coefficient of linear regression
R_a	arithmetic average of roughness (μm)
R_q	root mean square of roughness (μm)
s	curvilinear abscissa (mm)
S_c	crack area (mm^2) at the initiation
$\boldsymbol{T}$	traction vector
u_j	displacement (mm) of adherend j in the x direction
U_e	element nodal displacement vector
V_j	shear force (N) in adherend j in the y-direction
w_j	displacement (mm) of adherend j in the y-direction
W_c	dissipated energy of three-point bending test (mJ)
ΔZ	height variation (mm) of the roughness profile
θ_j	bending angle (rad) of the adherend j about the z-direction
ν	Poisson's ratio
ν	Strain energy density
σ	interfacial peel stress (MPa)
$\boldsymbol{\sigma}$	stress tensor
σ_c	interfacial tensile stress (MPa)
σ_{eq}	equivalent stress (MPa)
τ	interfacial shear stress (MPa)
τ_c	critical shear stress (MPa)
$\mathcal{G}$	differential energy release rate (N/mm)
$\mathcal{G}_c$	fracture toughness (N/mm)
$\mathcal{G}_{inc}$	incremental energy release rate (N/mm)
$\mathcal{G}^{I}_{dif}$	mode I component of incremental energy release rate (N/mm)
$\mathcal{G}^{II}_{dif}$	mode II component of incremental energy release rate (N/mm)
$\mathcal{G}^{III}_{dif}$	mode III component of incremental energy release rate (N/mm)
(x,y,z)	global reference system of axes (mm)
3PBT	three-point bending test
CC	coupled criterion
DOF	degree of freedom
DETA	diethylenetriamine
DGEBA	polyepoxide bisphenol A diglycidyl ether
FE	finite element
ME	macro-element
ST	surface treatment
VCCT	Virtual Crack Closure Technique

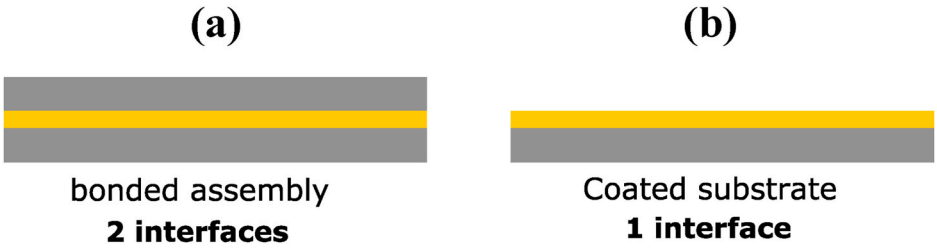

Fig. 1. The number of interfaces for each bonded assembly configuration.

assembly focused on a single interface (see Fig. 1-b). Both coated and uncoated specimens have similar fracture mechanisms. As the coating thickness tends to zero, it becomes an uncoated configuration.

The three-point bending test's crucial advantage is often providing an identifiable zone for interface debonding initiation [9,10]. In other cases, a clear discernment of initiation and propagation is impossible, depending enormously on the ST [9]. Mittal (1978) [10] classified the failure initiation in three categories for a painted substrate:

- type "a" for interfacial failure
- type "c" for cohesive failure
- type "i" for interphasial failure

By definition, an interfacial failure takes place within the first bonded layer and exists only in theory. On the other hand, a cohesive failure occurs when the adhesive is separated from the substrate on an adhesive layer sufficiently far from the interface (the properties do not vary through the adhesive thickness). The third possibility is an interphasial failure when the adhesive separates from the substrate on a layer whose properties differ from the bulk polymer. Roche et al. (1982) [7] and Sauvage et al. (2017) [9] noticed the dependency between the critical force (F_c) of the 3PBT and the ST. However, the experiments did not conclude how the fracture mechanisms of initiation and propagation were related to adherence.

Roche et al. (1982) [7] proposed five categories of propagation behaviour: i – without failure, ii – brittle failure, iii – smooth and rapid failure propagation, iv – Smooth and slow failure propagation and v – stepwise failure propagation. Up to now, no relation among the failure initiation, failure propagation and adherence measurements, such as the critical force obtained via a load cell, was shown in the literature. Then, a question arises: Can we take advantage of interfacial properties to avoid unexpected failure and somehow control the failure propagation

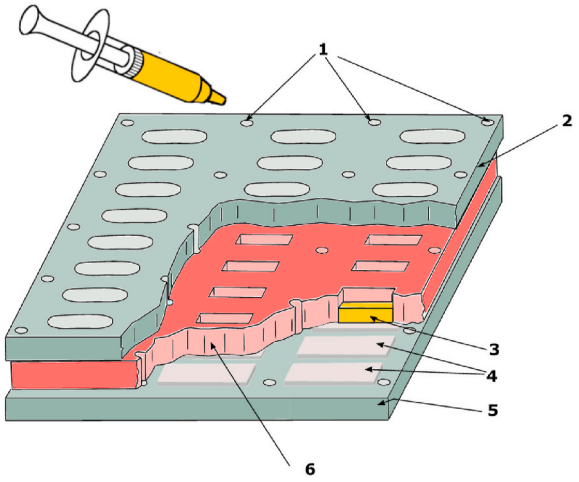

Fig. 2. Manufacturing of samples according to ISO 14679-1997 [8] (1 – bolts, 2 – faster plate, 3 – adhesive, 4 – substrate, 5 – lower plate, 6 – silicone mould).

to get safer structures?

In this paper, the adherence of aluminium alloy 2024-T3 and an adhesive DGEBA/DETA™ was evaluated using the 3PBT. The samples were prepared under different conditions such as ST, time lag at room temperature, adhesion promoter concentration, and curing temperature. Hence, an extensive experimental database was used for determining the energy release rate and critical stress using the coupled criterion, which resulted in an adhesive/cohesive criterion for the three-point bending test.

2. Experimental test

2.1. Materials

The samples comprised of an aluminium alloy 2024-T3 laminated substrate, with two different thicknesses – 1.08 mm and 1.62 mm, supplied by Rocholl GmbH and an adhesive polyepoxide bisphenol A diglycidyl ether (DGEBA), functionality 2, supplied by DOW Chemical, whereas SIGMA–ALDRICH supplied the amine diethylenetriamine (DETA) – functionality 5. For some cases, an adhesion promoter, the organosilane GLYMO (3-Glycidyloxypropyl)trimethoxysilane – functionality 1, also supplied by SIGMA-ALDRICH, was also included directly into the organic resin, in two different ratios - 5% w/w and 1% w/w. Their respective molar masses are M_{DGEBA} *340.41 g*, M_{DETA} *170.30 g* and M_{organ} *236.34 g*. The adhesive was produced by mixing the epoxy and the amine at room temperature. If desired, the adhesion promoter was first mixed with the epoxy until a homogeneous phase was formed, and then the amine was included, mixing again at room temperature. Finally, the blend was poured into the mould, as shown in Fig. 2.

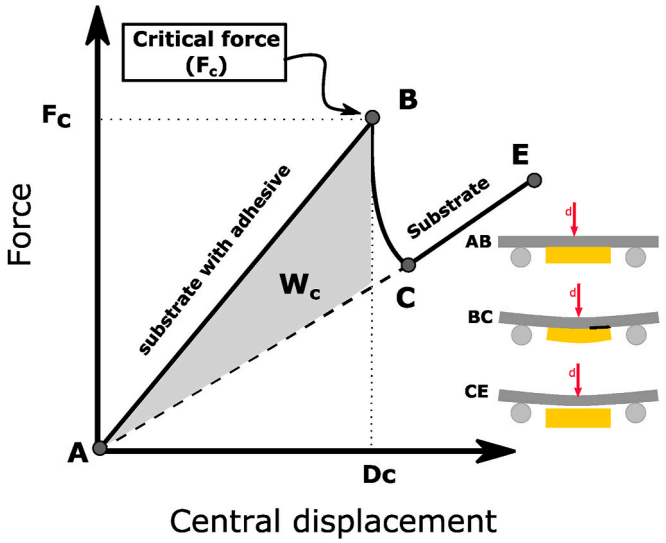

Fig. 4. Example of the three-point bending curve: AB – specimen stiffness; B – instantaneous failure initiation; BC – Failure Propagation; CE – substrate stiffness.

The polymerisation cycle was performed under the following conditions: the specimens stayed a few hours at room temperature (time lag), a gradual increment until the set-point temperature 140 °C. The sample remained 1 h at the set-point temperature and declined progressively, avoiding residual stresses.

2.2. Surface treatments

In order to understand the substrate/adhesive interactions, different STs were considered as follows:

I. Acetone degreasing
II. Acetone degreasing + HNO_3 at room temperature for 2 min
III. Acetone degreasing + HNO_3 at 50 °C for 10 min

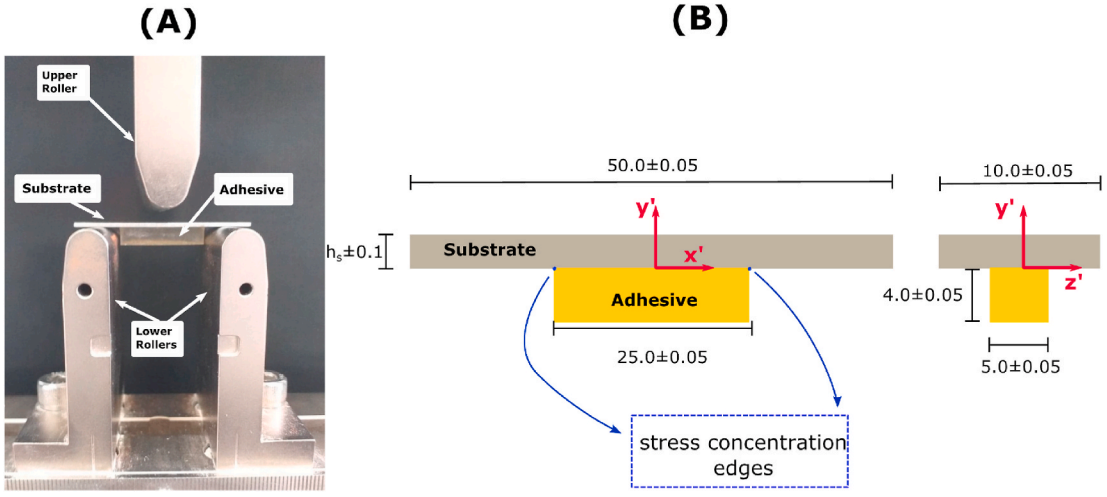

Fig. 3. (a) Three-point bending apparatus (b) Dimensions according to ISO 14679-1997 [8].

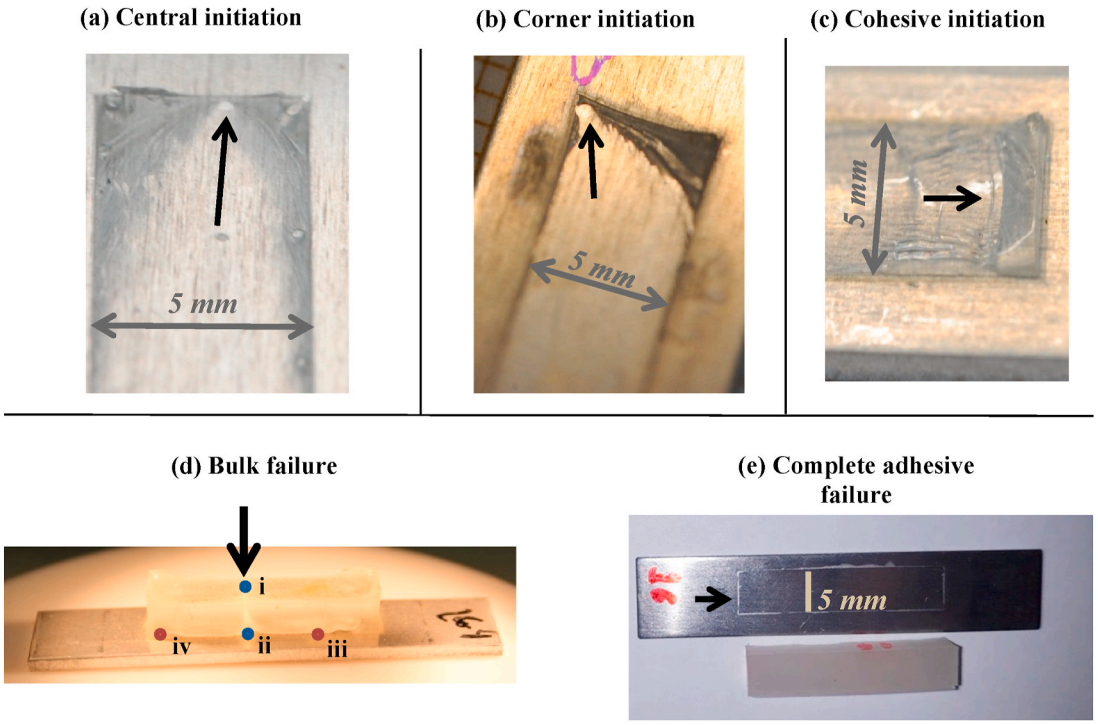

Fig. 5. Classification of failure initiations using a visual criterion: (a) central adhesive failure, (b) corner adhesive failure, (c) cohesive, (d) bulk and (e) complete adhesive failure. The black arrows indicate the initiation zone.

IV. Acetone degreasing + HNO_3 at 50 °C for 10 min + H_2O at 100 °C for 30 min.

After each acid etching, the use of deionised rising water freed the HNO_3 exceeding.

For an optimal bonding condition using an organosilane, Abel (2011) [11] listed many parameters which can affect the adherence, such as the concentration of organosilane, time lag at room temperature, temperature. The authors indicated that the purpose of the study is to merely provide different adherence levels instead of seeking the perfect condition to enhance adherence.

2.3. Three-point bending test (3PBT)

The 3PBT uses a substrate bonded directly on a thick adhesive stiffener element ($25 \times 5 \times 4$ mm^3), as shown in Fig. 3, according to ISO 14679-1997 [8]. A debonding occurs because of a stress concentration near the inner adhesive-substrate edges, as shown in Fig. 3.

Test campaigns were carried out using an INSTRON tensile machine 3367 (INSTRON SA, France), equipped with three-bending rollers. The upper roller imposed a controlled displacement (0.5 mm/min), while the corresponding load was recorded by a 5 kN load cell. The key features of a traditional response are shown in Fig. 4: first, the displacement reaches a critical value, in which failure initiates (point B). Then, a sudden drop in load (Fc) takes place in the period of adhesive debonding. Finally, the remaining behaviour shows only the substrate stiffness (CE). Critical force is directly dependent on the substrate thickness, which means the thicker is the substrate, the greater the critical force.

The energetic representation of adhesive failure is also shown in Fig. 4, as defined by Roche et al. (1994) [12]. The dissipated energy (W_c) of the three-point bending test is equivalent to the subtended area between the standard specimen and only the substrate. In his proposition, Roche stated that the energy should be independent of the bonded region width or substrate compliance. The computation of the subtended area:

$$W \quad F_c D_c/2 \quad k_{subst} D_c^2/2 \tag{1}$$

where k_{subst} is the substrate stiffness.

2.4. Post-mortem analysis

By definition, an interface debonding takes place precisely when the substrate-adhesive (covalent/ionic/weak) bonds are broken. Therefore, the theoretical definition operates only for model surfaces, when the roughness yields to zero.

The model surface is not a simple task to get, even less with a surface treatment. Watts (2011) [13] described an interfacial metal failure surface from an adhesively bonded aluminium test. He showed small islands of adhesive, which is interpreted as an interfacial failure, reaching a maximum size up to around 100 μm, for a blasted substrate with 50 μm alumina grit. Watts had also stated the complex mission of characterising failures, depending strongly on the level of the assessment methods available. For this study, a 3D map scanning was performed by the mechanical Profilometer DektakXT Stylus (Bruker Corporation). In such a test, the roughness was evaluated immediately after the surface treatment. Finally, the identification of the failure initiation and propagation zones was carried by the high definition camera Nikon D3 and the optical microscope Wild Makroscop M420.

3. Characterisation of failure initiation and propagation

3.1. Failure initiation analysis

The adhesive failure classification adopted a visual criterion: adhesive initiation (central or at the corner), cohesive initiation, bulk failure and complete adhesive failure, as shown in Fig. 5. When the identification of the small round zone at initiation was possible, the crack surface was measured. The differentiation of failure initiation and propagation for cases (c) and (e) are not possible. However, the failure

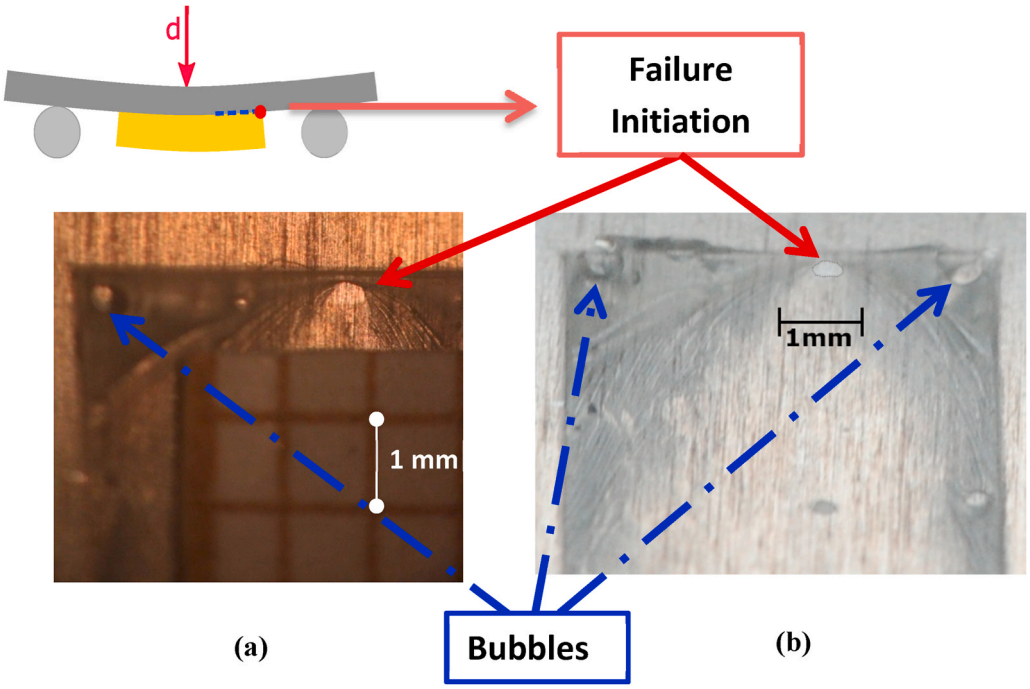

Fig. 6. Initiation of interface debonding of the sample: (a) Optical micrograph using artificial lights and (b) high definition camera using natural light.

Table 1
Small round measurement using the high-definition camera (Nikon D3) and the microscope (Wild Makroskop M420).

Substrate thickness	Camera (sunlight)	Microscope (artificial lights)
1.08 mm	0.070 ± 0.02 mm^2	0.069 ± 0.02 mm^2
1.62 mm	0.040 ± 0.01 mm^2	0.038 ± 0.01 mm^2

initiation and propagation for the case (e) are adhesive, and for this reason, the entire overlap region was supposed to correspond to the interface initiation surface (125 mm^2).

In the point of view of failure initiation shown in Fig. 5, both cases (c) and (d) are cohesive failures, but the cracks ignite in different positions. For case (d), the crack initiates at the top of the bulk polymer - point (i) – and it moves towards the interface – point (ii). When the crack tip reaches the aluminium interface, the crack propagates in two directions – points (iii) and (iv). On the other hand, the cohesive failure presented

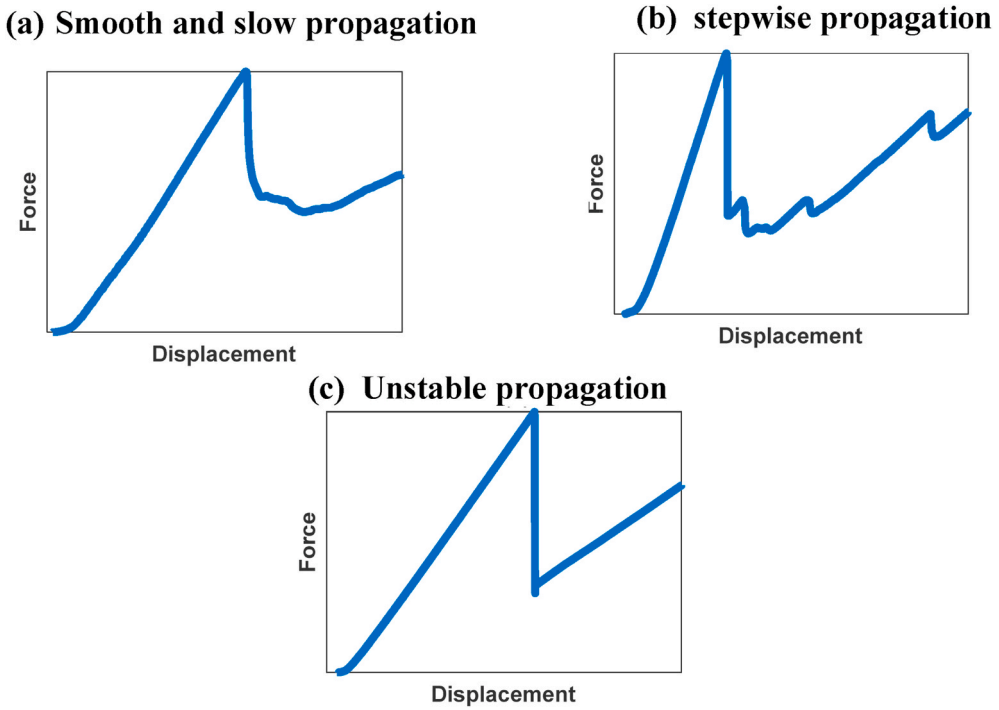

Fig. 7. Classification of failure propagation in three categories: (a) smooth and slow propagation (b) stepwise propagation (c) unstable propagation. All curves were obtained from the 3PBT campaign presented in this paper.

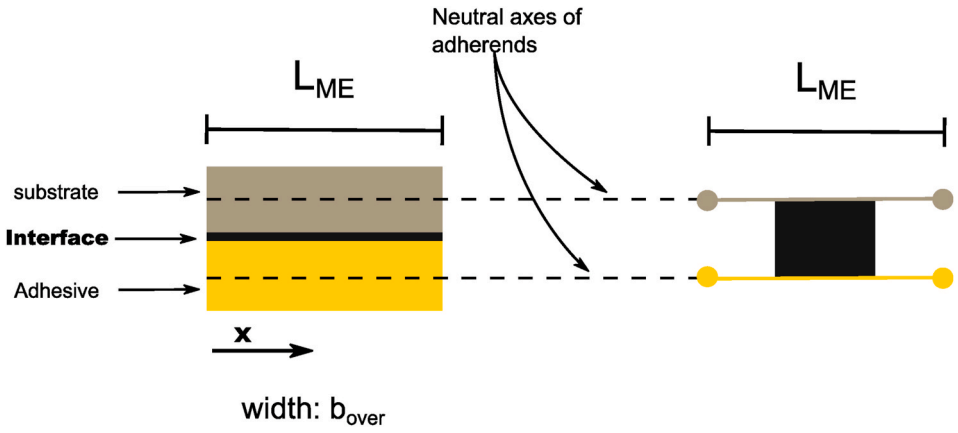

Fig. 8. Macro-element representation of aluminium substrate, interface and bulk adhesive.

in case (c) ignites near the interface, and the crack tip propagates in only one direction. Besides, after the critical force, the overall stiffness becomes greater for case (d) than for case (c), because of the debonding of a large region for case (c). The remaining stiffness for case (d) reduces gradually until the substrate stiffness till the full debonded surface appears.

As briefly introduced in Section 2.4, two different optical systems were available to assess the failure initiation zone: The high definition camera (Nikon D3) and the optical microscope (Wild Makroscop M420). Hence, a representative case of adhesive failure initiation was measured for both methods, as shown in Fig. 6. Even if some bubbles may eventually appear only in the bulk adhesive, a central round area is indicated.

The initiation areas (as those shown in Fig. 6-a and 6-b) were calculated using ImageJ, an open-source image processing program. The measurements of small round areas following both techniques are reported for both substrate thicknesses in Table 1. It is shown that (i) the measurement of both techniques are in close agreement and (ii) the standard deviations are very low. Indeed, identifying the initiation surface using the camera and the sunlight is much more practical and comfortable than using the optical microscope. Birro et al. (2020) [14] also evaluated the robustness of the measurement technique and the error associated with the critical energy release rate and critical stress. The study concluded a minor impact on both properties.

Although named as central failure initiation, the small round zone appeared over two-thirds of central width, instead of the half-width [9].

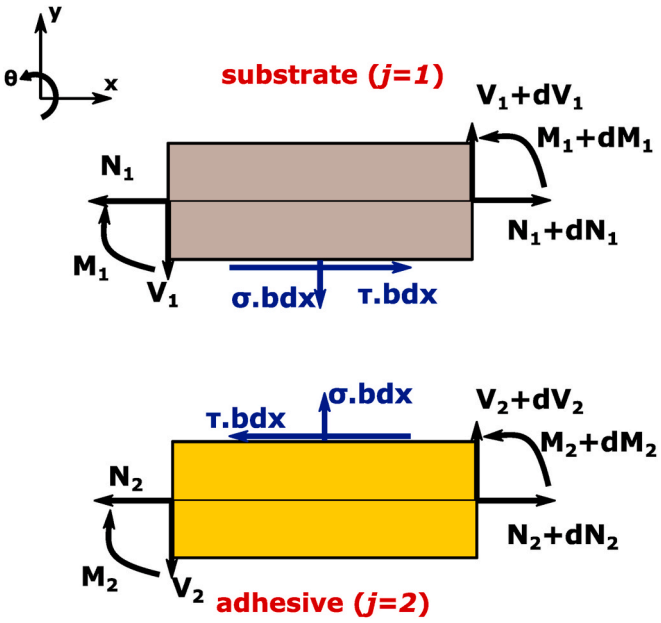

Fig. 9. Local equilibrium of an infinitesimal bonded element.

3.2. *Classification of failure propagation*

Roche et al. (1982) [7] proposed five categories for the propagation behaviour: i – without failure, ii – unstable propagation, iii – smooth and rapid failure propagation, iv – Smooth and slow failure propagation and v – stepwise failure propagation. After visual evaluation of all propagation responses, the current analysis showed a similar behaviour (see Fig. 7): (a) smooth and slow propagation (b) stepwise failure (c) unstable propagation.

4. Coupled criterion with macro-element analysis

4.1. *1D-beam macro-element analysis*

For a complete interfacial analysis, the numerical computation helps the assessment of the interfacial properties, such as the critical stress and the fracture toughness. For this purpose, the semi-analytic macro-element (ME) can be used to determine the response of the 3PBT. The ME was initially inspired by the Finite Element (FE) method. In order to model a bonded overlap in the frame of the ME technique, adhesive and substrate are considered as beam linked at their interface by a bed of shear and peel springs [15]. The authors used this last approach for the interface modelling to simulate a 3PBT up to failure. It has already been successfully used for the simplified stress analysis of bonded joints up to failure [15] as well as for the simulation of the delamination of composite laminates [16].

On the other hand, the ME does not assume interpolation functions, as classically performed by the FE. In fact, these interpolation functions are based on the solution of the governing differential equations [14]. Thus, a single ME can be applied to mesh an entire bonded overlap for a linear elastic analysis. The 1D-beam ME has four nodes, and each node has 3° of freedom: 2 translations and one rotation. A representation of a ME is shown in Fig. 8, defined with the length L_{ME} and the overlap width b_{over}.

As shown in Equation (2), the governing equations are based on the global equilibrium of adhesive, substrate and interface (see Fig. 9). Here, both substrate and adhesive are homogeneous linear elastic, with a

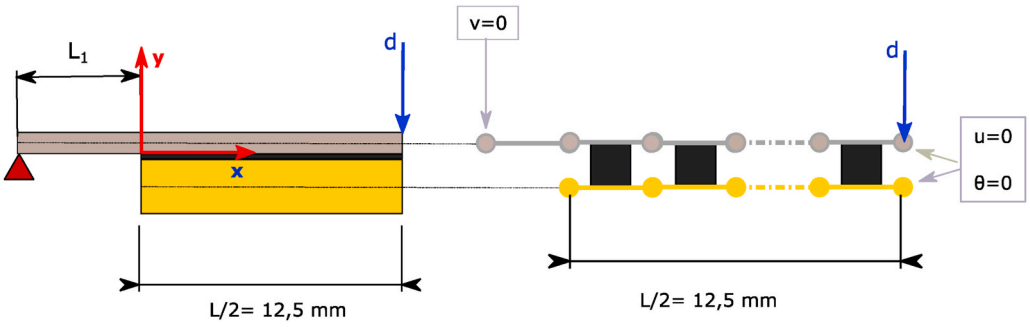

Fig. 10. Boundary conditions of the numerical simulation.

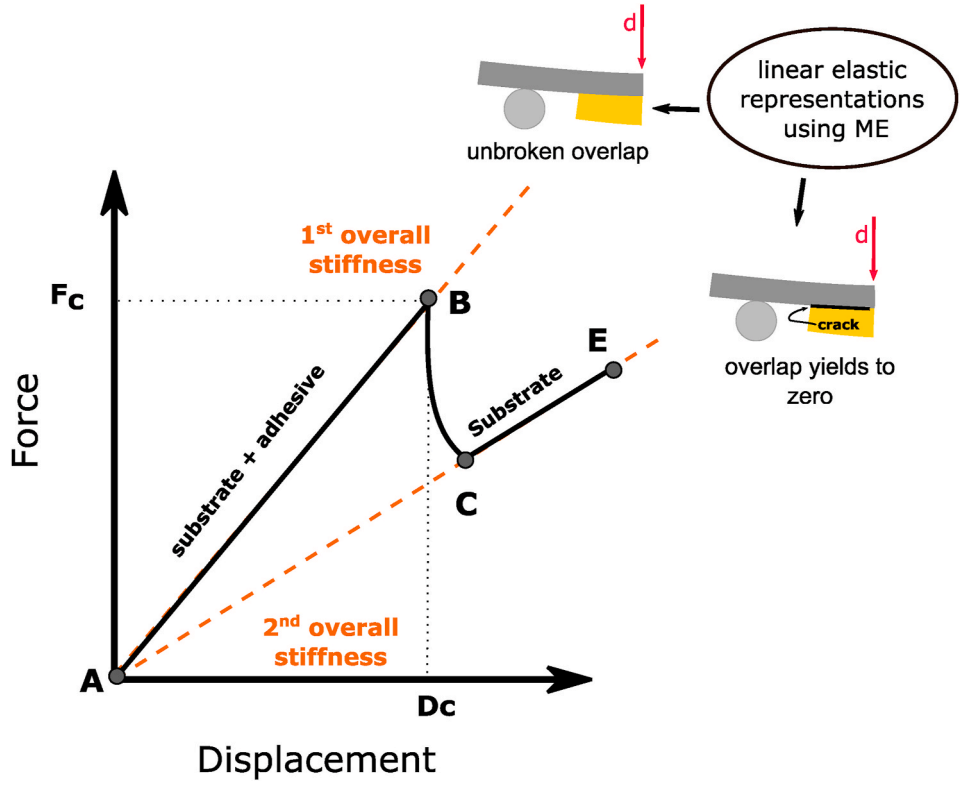

Fig. 11. Linear elastic representation using ME of the first and the second overall stiffnesses.

rectangular cross-section of thickness h_j and width b_j, where the subscript j indicates 1 and 2 for substrate and adhesive, respectively.

$$\begin{cases} \dfrac{dN_j}{dx} & (\ \ 1)^j \sigma b_{over} \\ \dfrac{dV_j}{dx} & (\ \ 1)^{j+1} b_{over}\tau \qquad , j \quad 1,2 \\ \dfrac{dM_j}{dx} + V_j + \dfrac{b_{over}h_j\tau}{2} & 0 \end{cases} \tag{2}$$

where N_j *is* the normal force, V_j is the shear force and the M_j bending moment of adherend j. Moreover, the interfacial peel stress is denoted as σ, and the interfacial shear stress is denoted asτ. In the frame of 3PBT, the global equilibrium requires applying the overlap width b_{over} defined as b_{over} $\min(b_1,b_2)$.

Under the assumption of laminated Timoshenko beams for the substrate and adhesive, the constitutive equations are:

$$\begin{cases} N_j & A_j\dfrac{du}{dx} \quad B_j\dfrac{d\theta_j}{dx} \\ V_j & H_j\left(\dfrac{dw_j}{dx} \quad \theta_j\right) \quad ,j \quad 1,2 \\ M_j & B_j\dfrac{du_j}{dx} + D_j\dfrac{d\theta_j}{dx} \end{cases} \tag{3}$$

where A_j, D_j, H_j and B_j are the membrane, bending, shear and coupling stiffness, respectively; u_j is the displacement (mm) of adherend in the x-direction; w_j is the displacement (mm) of adherend in the y-direction; θ_j is the bending angle in the adherend, and the index j indicates the adherend.

The interface is considered as an infinite number of shear and peel springs. In such a case, the shear and peel stresses were expressed, respectively, as follows:

$$\tau \quad k_{II}\left[u_2 \quad \frac{h_2\theta_2}{2} \quad \left(u_1 + \frac{h_1\theta_1}{2}\right)\right] \quad k_{II}\Delta u \tag{4}$$

$$\sigma \quad k_I[w_1 \quad w_2] \quad k_I \Delta w \tag{5}$$

where k_I and k_{II} are the peel and shear intefacial stiffnesses, respectively. Birro et al. (2020) presented the details of the elementary stiffness matrix [14].

Finally, the three-point bending specimen is transformed to the assembly of macro-elements bricks, as shown in Fig. 10. The two adherends correspond to the aluminium plate and the bulk adhesive. The analysis comprised a symmetric geometry, fixing the y-displacement on the left, as well as the rotation and the x-displacement in the symmetric axis. The overlap length was L 25 mm.

The outer length L_1 adjustment could overcome and adapt the physical boundary condition and the ME model - two cylinders in contact with the aluminium substrate versus a pinned support beam [14]. As shown in Fig. 11, the outer length L_1 regulates the second overall stiffness, which does not depend on the interface adjustment stiffnesses (k_I, k_{II}), as already stated by Birro et al. (2020) [14]. The second overall stiffness represents an overlap yielding to zero. On the other hand, the first overall stiffness – an unbroken overlap - (see Fig. 11), depends directly on the outer length L_1 and the adjusted interfacial stiffnesses (k_I, k_{II}). Hence, once L_1 is already set up, the next step consists of setting up k_I and k_{II}.

4.2. Coupled criterion (CC) analysis

The coupled stress and energy criterion proposed by Leguillon (2002) [17] is a viable alternative to the assessment of adhesive-to-substrate interface properties. The coupled criterion successfully solved many cases involving the stress concentration and interface debonding, including three 3PBT [14]. In summary, Carrere et al. (2015) [18] explained the CC's physical point of view: a stress criterion ensures that micro-cracks appear, while the energy criterion is responsible for propagating micro-cracks up to a macroscopic crack.

Based on the finite fracture length represented by the area S, the incremental energy release rate was calculated as:

$$\mathscr{G}_{inc} \quad \frac{\Delta W}{\Delta S} \geq \mathscr{G}_c \tag{6}$$

The development of the energy criterion considers a finite fracture length rather than the differential energy release rate of Griffith's theory $\mathscr{G}$ $-dW/dS$. As shown in Equation (7), the relation between the incremental and differential energy release rates is:

$$\mathscr{G}_{inc} \quad \frac{1}{\Delta S} \int_{S}^{S+\Delta S} \mathscr{G}(\Omega) \mathrm{d}\Omega \tag{7}$$

The stress criterion defines the second condition, in which the stress across the cracked surface had exceeded the critical stress, given as in Equation (8).

$$\sigma_{eq}(\mathbf{x}) \geq \sigma_c \forall \, \mathbf{x} \in S \tag{8}$$

The equivalent stress, as proposed by Martin et al. (2016) [19], was:

$$\sigma_{eq}(\mathrm{x}, \quad \mathrm{y} \quad 0) \quad \sqrt{\left(\frac{\sigma(x, y \quad 0)}{\sigma_c}\right)^2 + \left(\frac{\tau(x, y \quad 0)}{\tau_c}\right)^2} \geq 1 \; \forall \, x \leq a \tag{9}$$

Following the same hypothesis defined by Birro et al. (2020) [14] and Martin et al. (2016) [19], no mode differentiation is assumed (σ_c τ_c), and then, the equivalent stress was determined via Equation (10).

$$\sigma_{eq}(\mathrm{x}) \quad \sqrt{\sigma^2(x) + \tau^2(x)} \geq \sigma_c \; \forall \, x \leq a \tag{10}$$

Birro et al. (2020) [14] stated that no mode differentiation's assumption could not be supported in the frame of the fracture of bonded joints or the composite laminated materials. Thus, the validity of this hypothesis should be addressed for the interface crack debonding.

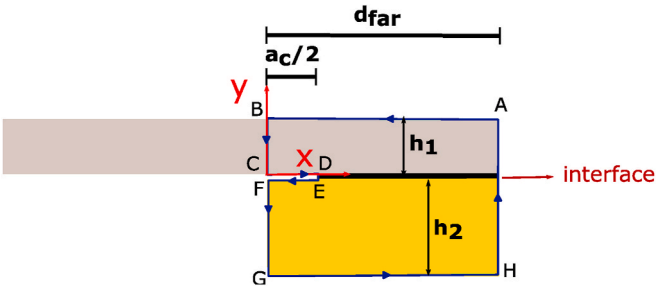

Fig. 12. The J-integral path over the cracked three-point bending specimen.

In Equations (6) and (8), the upper and lower bounds for the critical crack length (a_c) are defined. In the direct and more exploited application of the CC, the mechanical properties of materials are known. The goal is to reach the lowest load that satisfies both conditions the corresponding crack length [20]. However, the critical force (F_c) and critical crack length (a_c) were determined experimentally using 3PBT. Hence, these experimental parameters were applied to perform an inverse analysis, which implied the direct determination of the critical stress and fracture parameters of the initiation of interfacial debonding, Equations (6) and (10), respectively.

Finally, both stress and incremental energy release rate were obtained using the ME technique, assuming a linear elastic behaviour for the substrate and adhesive. A half crack length $a_c/2$ was introduced at each side in a symmetric model. Finally, the domain of integration of $\mathscr{G}_{\mathrm{inc}}$(see Equation (7)) was split into 200 parts, from 0 to $a_c/2$.

Moreover, no plastic deformation was verified when all the second overall stiffnesses (see Fig. 11) were analysed, and by consequence, the substrates did not deform plastically. Moreover, the non-formulated bulk adhesive is a pure brittle material. At this point, the authors cannot distinguish the adherence from possible dissipated energy. For simplification, the determination of the energy release rate is based on linear elastic analysis for adhesive and substrate (presumption of the coupled criterion). Thus, the method does not distinguish plasticity or other dissipative energies from adherence during failure initiation.

4.3. Energy release rate computation using J-Integral

The determination of the energy release rate used the J-integral, as proposed by Fraisse and Schmit [21]:

$$J \quad \int \Pi dy \quad \boldsymbol{T} \frac{\partial \boldsymbol{u}}{\partial x} ds, \; \boldsymbol{T} \quad \boldsymbol{\sigma} \cdot \boldsymbol{n} \tag{11}$$

where $\boldsymbol{u}$ represents the displacement vector, $\boldsymbol{T}$ represents the traction vector, Π is the strain energy density, s is the curvilinear abscissa, and finally, $\boldsymbol{n}$ represents the normal vector. The J-integral was applied over to the closed path ABCDEFGHA (see Fig. 12). Hence, the differential energy release rate was computed as originally proposed by Fraisse and Schmidt (1993) [21] and applied in the frame of interface crack debonding by Birro et al. [14], as follows:

$$J \quad \frac{1}{2b_{over}} \left[\frac{1}{A_1}\left(N_1^2 \quad N_1'^2\right) + \frac{1}{D_1}\left(M_1^2 \quad M_1'^2\right) + \frac{1}{H_1}\left(V_1^2 \quad V_1'^2\right)\right] + \frac{1}{2b_{over}} \left[\frac{1}{A_2}\left(N_2^2 \quad N_2'^2\right) + \frac{1}{D_1}\left(M_2^2 \quad M_2'^2\right) + \frac{1}{H_1}\left(V_2^2 \quad V_2'^2\right)\right] + 1 \Big/ b_{over}\left[V_1\theta_1 \quad V_1'\theta_1' + V_2\theta_2 \quad V_2'\theta_2'\right] \tag{12}$$

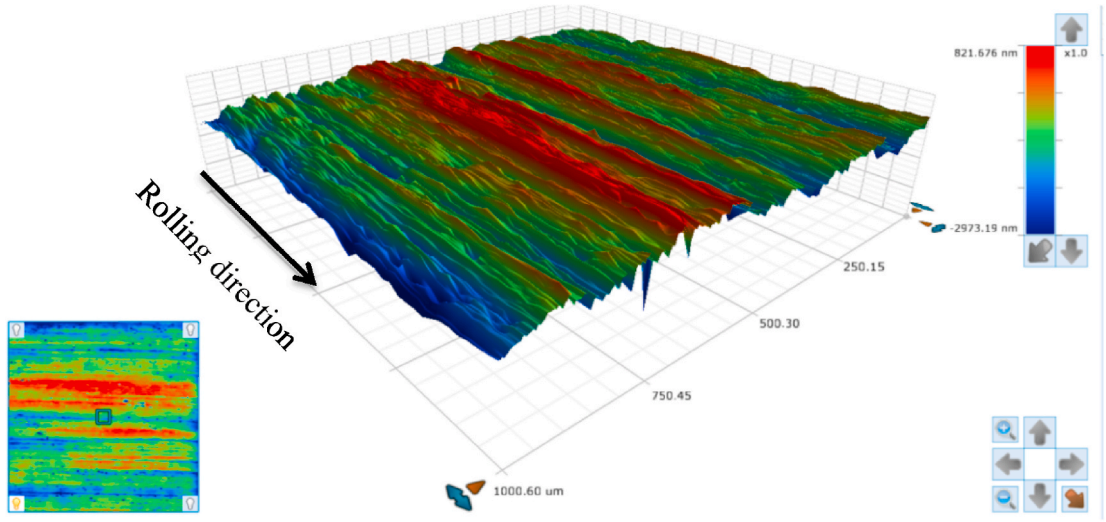

Fig. 13. 3D surface mapping (1 mm × 1 mm) after ST- III: average roughness R_a=0.156 µm.

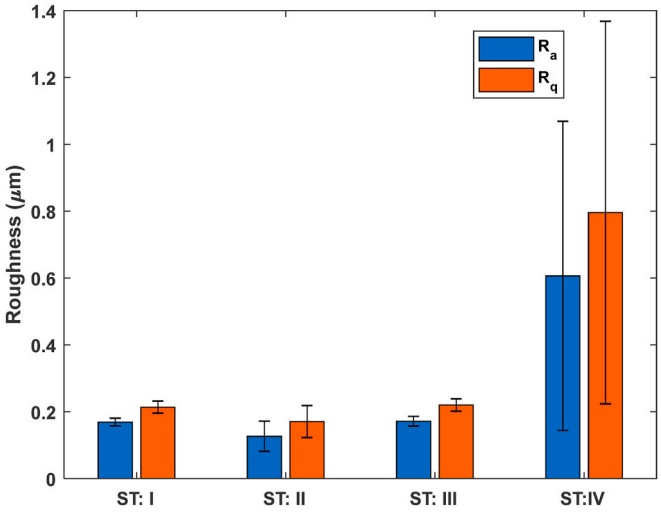

Fig. 14. Roughness evaluation for different STs.

where N_j, V_j and M_j were determined at $a_c/2$ (crack tip), while N'_j, V'_j and M'_j were determined at a distance d_{far} 0.4L (indicated in Fig. 12). Besides, all stiffness parameters were presented in Section 4.1. In particular, Fraisse and Schmit (1993) [21] stated a requirement for the cross-section HA: since the adhesive stress decreases exponentially, such a cross-section must be chosen far from the crack (d_{far}), so that it is not loaded – the imposed displacement is applied at x 0.5L.

As shown in Fig. 3, the adhesive and the substrate have different widths - b_a 5 mm and b_s 10 mm, respectively. The width discrepancy impeded a direct application of the J-integral, requiring a cross-section transformation. Hence, a new aluminium width b^*_s b_a and a new Young's modulus of substrate E^*_s $b_s{*}E_s/b_a$ were required, keeping unchanged the global stiffness of the specimen.

Birro et al. (2020) [14] applies the last step to smear the circular debonded area S_c into a symmetric narrow strip, introducing half crack length in each side of the specimen, as follows:

$$\frac{a_c}{2} \quad \frac{S_c}{2b_a} \tag{13}$$

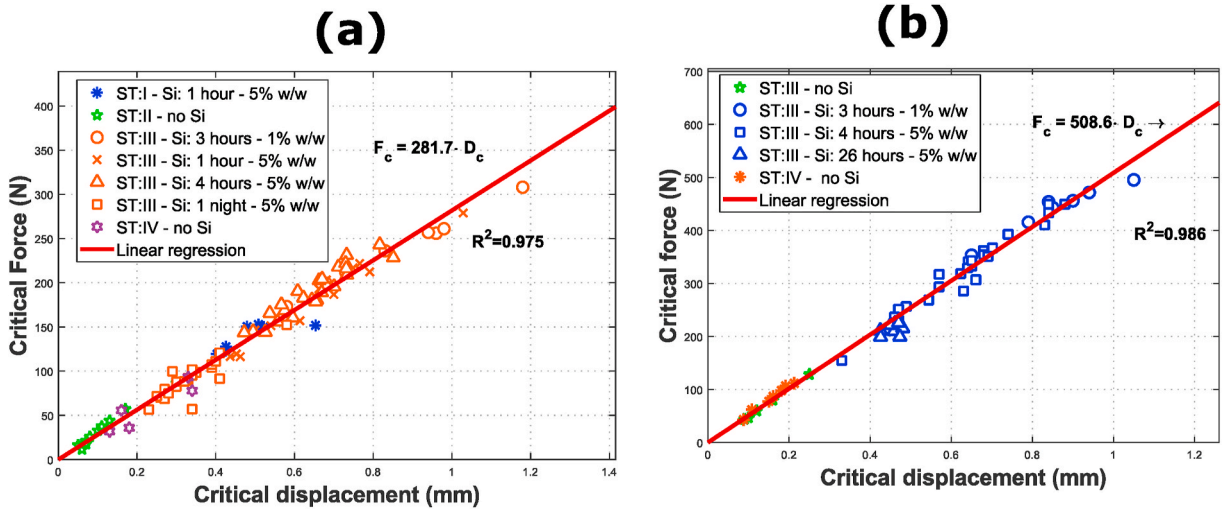

Fig. 15. Critical force versus critical displacement for different STs: (a) h_s=1.08 mm; (b) h_s=1.62 mm. (Legend - ST: surface treatment; Si: time lag at room temperature if the organosilane was included and organosilane concentration in w/w).

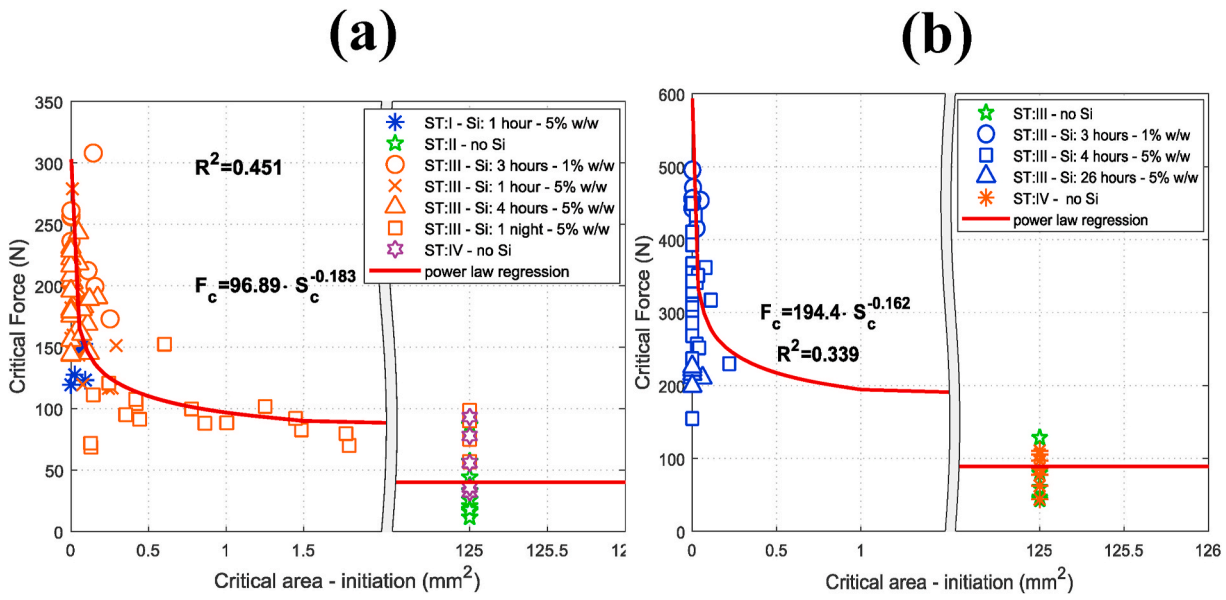

Fig. 16. Critical force *vs* critical area for different STs - (a) h_s=*1.*08 mm; (b) h_s=*1.*62 mm (Legend - ST: surface treatment; Si: time lag at room temperature if the organosilane was included and organosilane concentration in w/w).

5. Test results

5.1. Adhesive failure characterisation

In this proposition, the DektakXT Stylus profiler provided the 3D roughness mapping for different substrates in detail, as exemplified in Fig. 13.

The average arithmetic of roughness (R_a) and root-mean-square of roughness (R_q) of each substrate after exposure to an ST is indicated in Fig. 14. The ST-IV presented a high standard deviation and was not deeply explored since an accurate reproducibility was not obtained. The ST-IV was carried out as follows: the samples were first submitted to ST-III (nitric acid etching), followed by an immersion into a glass dish filled with water at 100 °C for 30 min. During the second step, bubbles appeared on the surface, resulting in a non-uniform ST, as shown by the high standard deviation.

The ST-III was the most exploited because of three fundamental reasons: a low standard deviation, ensuring great repeatability; excellent

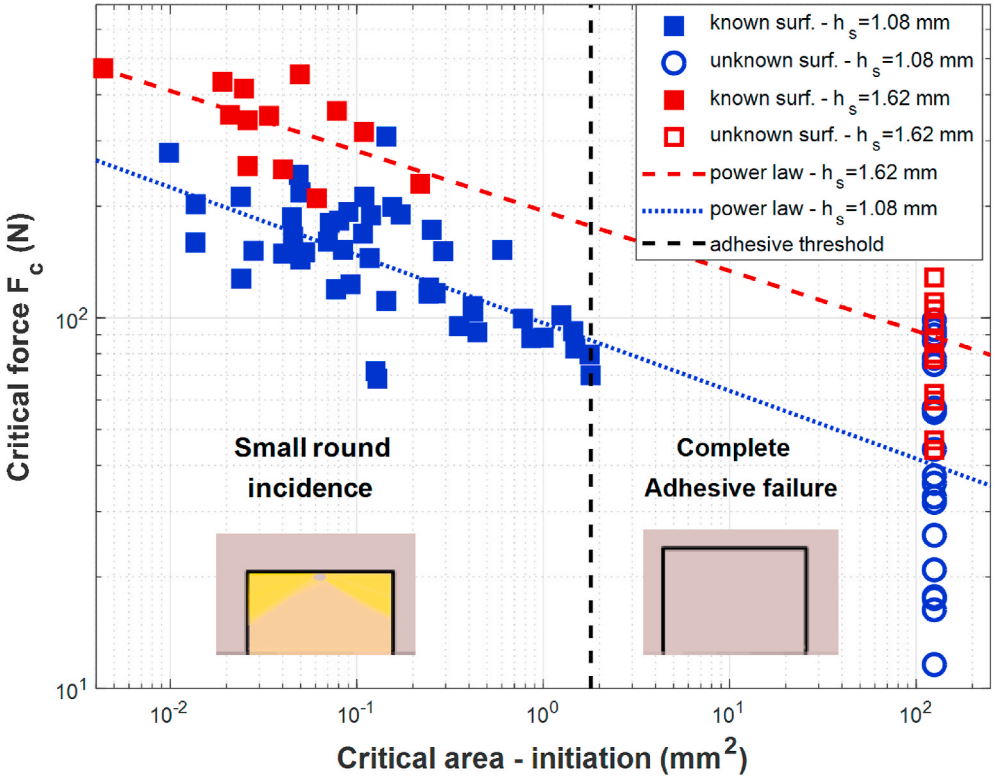

Fig. 17. The behaviour of fracture initiation in terms of critical force – Zone 1: Small round incidence of adhesive failure initiation; Zone 2: Complete adhesive failure (not possible to distinguish initiation and propagation).

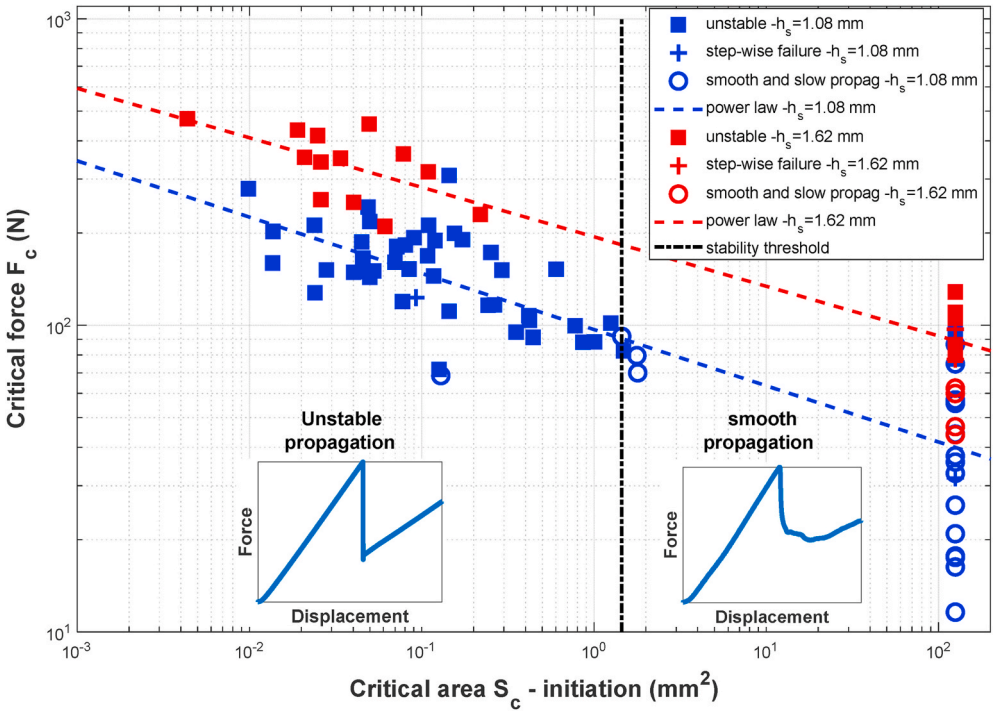

Fig. 18. Propagation fracture behaviour in terms of critical load – Unstable and smooth propagation.

feasibility, and easy identification of the failure initiation.

Although an interfacial debonding appears theoretically, a practical criterion was established to classify an interfacial debonding: a low adhesive residue can be readily confounded with roughness deviation. For this reason, hereafter, the practical criterion of interface debonding was established if the thickness of the residue adhesive layer on the substrate is lower than R_a. Moreover, Aufray and Roche [22] (2007) analysed the interphase between a DGEBA/DETA adhesive and aluminium structure. They examined the gradient of properties near the interface, corresponding to an interphasial thickness near 300 μm. Thus, hereafter, an interphasial debonding, indicates a thickness of the adhesive residues (e_{rem}) comprised from R_a to 300 μm.

5.2. *Three-point bending test results*

As previously stated in Section 2, the experimental configurations consider two different substrate thicknesses:

[1] Adhesive: DGEBA/DETA – substrate: AA 2024 T3 – *1*.08 mm in thickness
[2] Adhesive: DGEBA/DETA – substrate: AA 2024 T3 – *1*.62 mm in thickness

First, the critical force (F_c) and critical displacement (D_c) for both substrate thicknesses h_s and various STs were plotted for different conditions in Fig. 15. As expected, the ST did not affect the overall stiffness, as already demonstrated by Sauvage et al. (2017) [9]. Similarly, the organosilane concentrations affected F_c, whereas the experimental stiffness remains the same. The linear regression R^2 coefficient determined that the geometric distortion was minimised, as stated by Sauvage et al. (2017) [9].

Similarly, the F_c *vs.* S_c for each ST was also represented in Fig. 16, for both substrate thicknesses. The global behaviour revealed a remarkable threshold force in which a cohesive failure initiates when S_c yields to zero. Moreover, the critical force decreases as the critical area increases. Even if the tendency was similar for both substrate thicknesses, their different geometries impeded a direct comparison. A clear tendency was reported by the power-law regression, with a low R^2 for both cases. The authors highlight that the power-law regression has a merely qualitative representation of the global effects, which means an increase in F_c for low S_c and the asymptotic F_c tendency for high crack areas.

Hence, a unique power-law regression representing all STs and conditions helped a quick data manipulation estimate other properties instead of multiples power-law regressions for each ST and/or condition. The micro-cracks, bubbles or defects may also contribute to the increase in the deviation since the imperfections manifest themselves much more in a mesoscale (small-round surface) than in a macro-scale (force versus displacement).

Although the error is an intrinsic part of the data acquisition process, the authors opted not to represent the error bars of all parameters (F_c, D_c and S_c) of each sample since their values were usually less than the marker size (see Figs. 15 and 16).

5.3. *The general tendency of initiation and propagation of adhesive failure*

All the failure initiations were analysed and sorted by categories, according to the classification defined in Section 3.1. In general, the failure initiation analysis identified three different mechanisms: first, a cohesive initiation tendency is reached for high *Fc*, with a cohesive initiation or a bulk failure (See Fig. 5-c and 5-d). In such a case, the cohesive initiation was not presented in the log versus log plot in Fig. 17, as $S_c \to 0$. On the other hand, the second and third mechanisms were demonstrated in Fig. 17.

The graph showed in Fig. 17 was sorted in two different zones by a vertical dashed line, called “adhesive threshold line”, defining the most

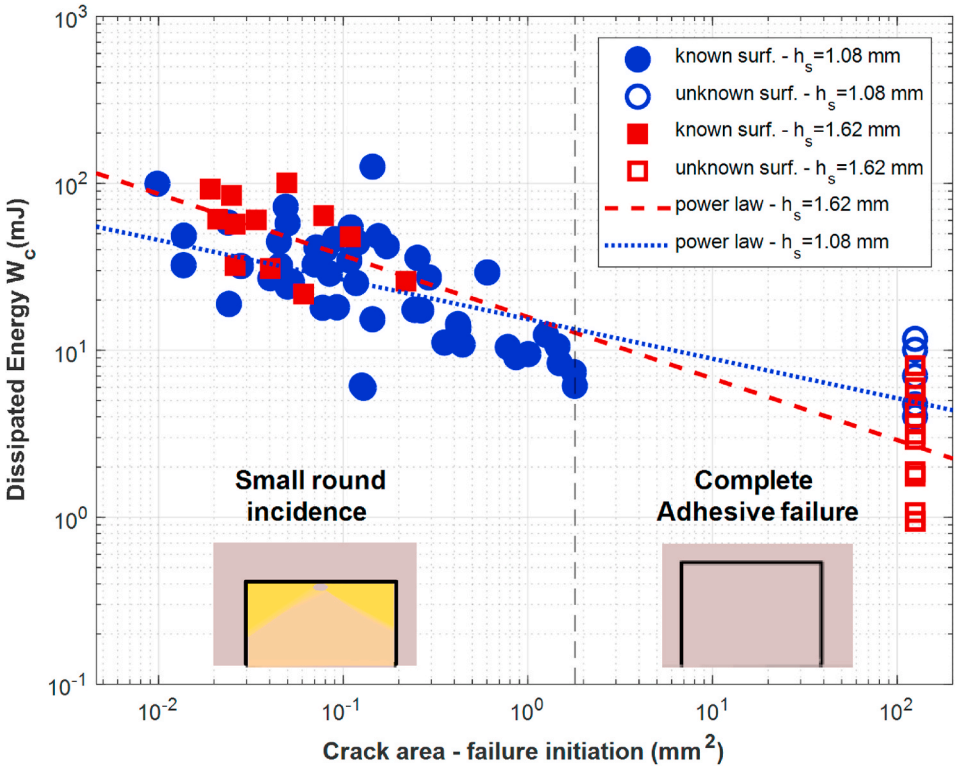

Fig. 19. The dissipated energy at the failure initiation defined by Roche et al. (1994) [12] for both thicknesses.

significant initiation area tracked by the optical devices ($S_c \sim 1.8$ mm^2). On the other hand, if the failure initiation area is indistinguishable from the failure propagation area, the sample is placed in a "complete adhesive failure" zone. Hence, the adhesive threshold line is interpreted as limiting, in which adhesive failure initiation cannot be anymore distinguished from adhesive failure propagation.

The first zone (on the left side – see Fig. 17) is labelled as "small round incidence", in which the failure initiation area could be directly tracked. In such a zone, the lowest area determined the cohesive-to-adhesive failure transition ($S_c \sim 0.005$ mm^2). More details were given in Appendix A.

The analysis of the load versus displacement responses for each sample also identified two different global regions in terms of stability, as shown in Fig. 18. First, an unstable propagation zone is defined for cohesive initiation and small round surfaces, which is comprised in the interval $0 < S_c < 1.45$ mm^2. The second region corresponded to a smooth propagation zone, defined by $S_c > 1.45$ mm^2. The stepwise failure was rarely observed and may be explained by defects or bubbles

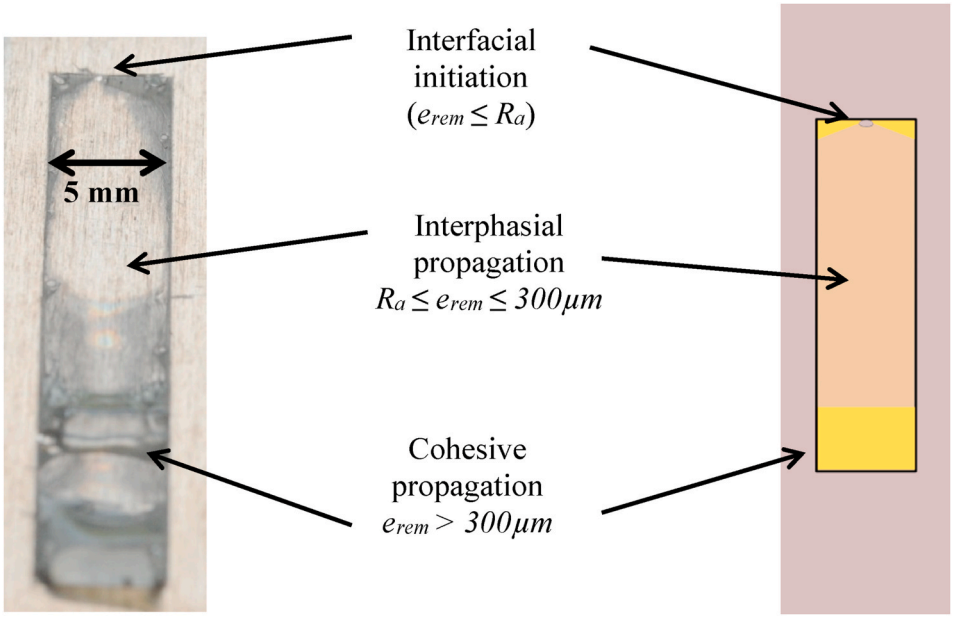

Fig. 20. Fracture behaviour in a post-mortem analysis of a sample present in zone 1 (see Fig. 19).

Table 2
CC Inputs and adjustment parameters calculated for each substrate thickness.

h_s (mm)	Input		Model adjustment parameters		
	F_c (N)	K_{spec} (N/mm)	L_1 (mm)	k_I	k_{II} (N/mm)
1.08	*96.9*Sc* $^{0.183}$	*298 ± 27*	*5.5*	*1710*	
1.62	*194.4*Sc* $^{0.162}$	*538 ± 27*	*5.5*	*1040*	

Table 3
Mechanical properties of substrate and adhesive.

	E (MPa)	ν
Adhesive	3000	0.35
Substrate	68,000	0.33

present in the substrate/adhesive interface.

Although very close, the stability and the adhesive threshold were not identical (see Figs. 17 and 18), defining a tight transition in which a smooth propagation and small round zone took place.

The authors have conducted a new study, and the preliminary results showed some benefits of introducing a pre-crack in the adhesive/substrate interface. The first results showed a significant F_c reduction, which placed the specimen in the stability zone (see Fig. 18). Moreover, the pre-cracks were an artificial method to overpass the stability threshold, facilitating the real-time crack measurement.

5.4. Assessment of W_c

The previous study [9,12] showed that the analytical methods are not reliable and dependent on the substrate thickness to describe the interfacial quantities, such as energy and stress. Moreover, applying the critical force as a global adherence indicator does not allow the comparison of different geometries [9,12]. Roche et al. (1994) [12] proposed an independent geometrical criterion, in theory, using the critical energy dissipated during failure initiation (Section 2.3). However, Roche calculated the dissipated energies for different substrate thicknesses, as the average values were different but always within a large margin of sampling error.

For a better understanding in this paper, the dissipate energy W_c at failure initiation was calculated for each sample, as indicated in Fig. 19. The results showed that the dissipated energy was not completely independent of the substrate thickness. However, a more accentuated influence of the substrate thickness was noticed for F_c rather than W_c, as expected (see Fig. 17).

In conclusion, the W_c was not a perfect parameter to represent the failure initiation. The discrepancy of both substrate thicknesses (see Fig. 19) showed that more phenomena were involved: the propagation comportment can indirectly contribute and overestimate the dissipated energy. When high F_c was present from the experimental results, the bulk adhesive completely separated from the substrate (brittle behaviour), whereas a progressive and smooth debond took place for low F_c. In short, in the frame of unstable propagation, the dissipated energy at failure initiation could not be disassociated from the dissipated energy at failure propagation (Fig. 7-c). To illustrate, Fig. 20 represents classical post-mortem analysis of a sample placed in the small round incidence zone and brittle behaviour: when the crack reaches the end of the overlap, the crack front advanced through the bulk polymer, contributing to the unstable comportment.

Finally, the analytical method did not distinguish the initiation and propagation phases of an unstable propagation since a complex fracture path was not represented in the model.

5.5. Numerical results

The computation of W_c in Section 5.3 allowed a preliminary comparison between two different substrate thicknesses. On the other hand, the overall dissipated energy method does not consider the crack length at initiation, which is a crucial fracture mechanics parameter. For this

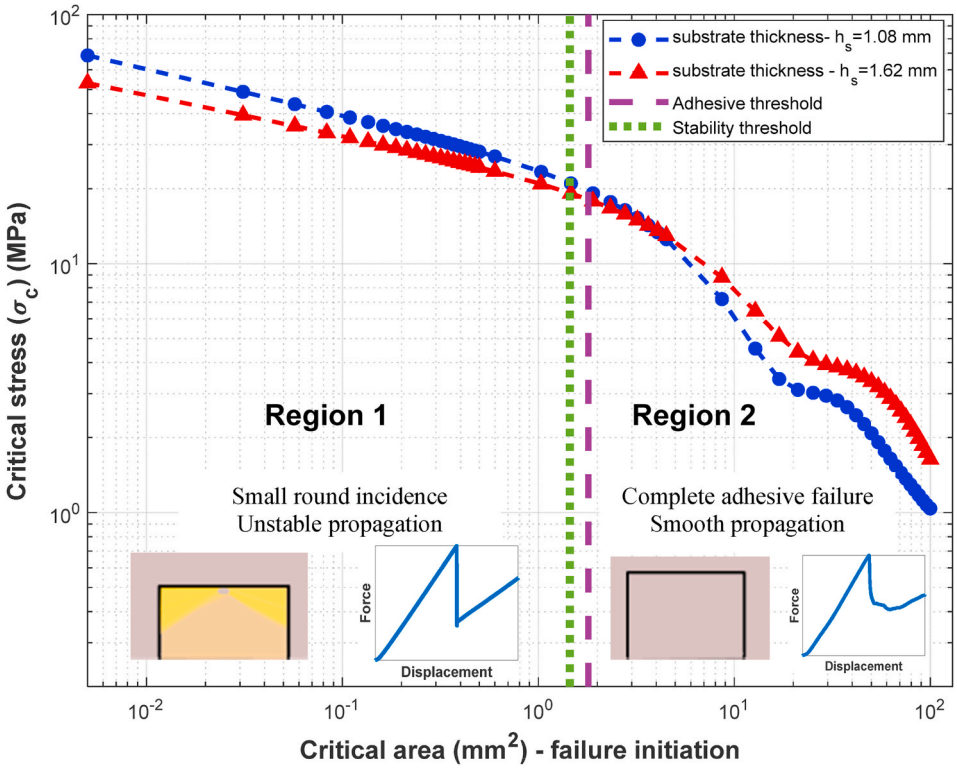

Fig. 21. Critical stress σ_c variations versus the critical area at the failure initiation – calculated via CC.

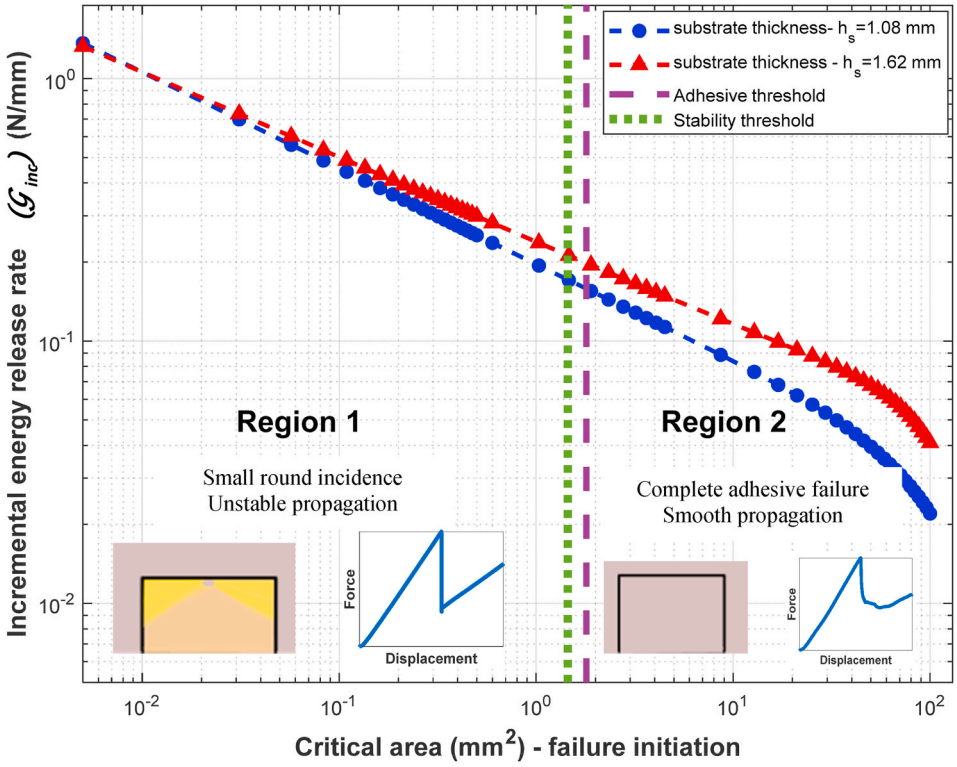

Fig. 22. Critical energy release rate $\mathscr{G}_{inc}$ variations versus the critical area at the failure initiation – calculated via CC.

reason, the CC was applied, using the fitted curves for both substrates to estimate the mechanical properties during the failure initiation. The power-law regression equations and the specimen stiffness K_{spec} were shown in Table 2 as input. The computation of K_{spec} used the least mean square over each force *vs* displacement curve of the first linear region. The Young's moduli of substrate and adhesive were listed in Table 3, as used by Birro et al. (2020) [14].

As demonstrated by Birro et al. (2020) [14], the fitted L_1 was substantially closer to the standard value L_1 5.5 mm for both cases. Moreover, the overall stiffnesses of the specimens are directly dependent on the interfacial adjustment stiffness k_I. Thus, for the specimen's overall stiffness, their corresponding k_I was calculated and listed in Table 2.

Finally, the critical stress (σ_c) and the incremental energy release rate ($\mathscr{G}_{inc}$) were computed and plotted in Figs. 21 and 22, respectively. As Birro et al. (2020) [14] mentioned, the critical stress had a high sensibility to the interfacial adjustment stiffness (see Fig. 21). On the other hand, the incremental energy release rate was less sensitive to the interfacial adjustment stiffness dissimilarity and ensured a good correlation of $\mathscr{G}_{inc}$(see Fig. 22). In conclusion, the mechanical properties of the interface were similar and independent of the substrate geometry.

Even if the critical force were divergent for the two-substrate thicknesses, a good convergence was obtained for the failure mechanism (failure initiation and propagation), the crack area at initiation and the stability behaviour for both substrate thicknesses. Indeed, both substrate thickness results could only be compared when the mechanical properties of the interface were determined, overcoming the previous issues from Roche [12] and Sauvage [9] (similar interfaces and different geometries). Thus, the application of the CC, enhanced by a detailed post-mortem analysis, provided a complete assessment of the mechanical properties of the interface and the overall behaviour of the interface crack debonding.

Moreover, the experimental observations could enrich the numerical analysis. The adhesive and stability threshold values (dotted green line and dashed purple line), presented in Figs. 21 and 22 revealed three global behaviours for mechanical properties of interface *vs* crack area at initiation:

- Region 1: Small round zone and unstable propagation – $0.005\ mm^2 < S_c < 1.45\ mm^2$
- Region 2: no presence of small round zone and stable propagation $1.8\ mm^2 < S_c < 125\ mm^2$

The lowest area value measured ($S_c \sim 0.005\ mm^2$) was also considered a threshold value for interface debonding. The initiation area yields to zero for high critical forces, corresponding to a cohesive failure.

However, even if this effect was experimentally observed, it could not be incorporated into the power-law regression (S_c *0*). The authors also observed a tight transition region (*1.45* $< S_c <$ *1.8* mm^2), in which a stable propagation and the small round zone were present simultaneously.

6. Conclusion

In this analysis, different parameters to represent and quantify the initiation of interfacial failures, such as roughness (R_a), critical load (F_c), critical area (S_c), dissipated energy (W_c), stress (σ_c) and incremental energy release rate ($\mathscr{G}_{\text{inc}}$) were studied.

First, a criterion for interface debonding initiation could be defined in terms of the average roughness R_a. It is shown that the two classical parameters of the 3PBT studied by Roche et al. (1994) [8], the critical force (F_c) and the overall dissipated energy (W_c), were not the best to represent the adherence even comparing similar interfaces. The assessment of W_c could not distinguish between the initiation and propagation contributions. Thus a more robust analysis is recommended: the CC applied to the 3PBT allowed a good agreement between the interfacial energy release rate in terms of S_c for both substrates. For both substrate adherence tests, $\mathscr{G}_{\text{inc}}$ is shown to be independent of the geometry, and this result was not trivial to demonstrate. The experimental fracture observation also enriched the numerical analysis: threshold values for cohesive/adhesive initiation and unstable/stable propagation were established for the interfacial parameters. Thus, this paper can be read as the first work towards the ability to predict interface failure. The presented methodology could be performed with other tests, which also provide interfacial failure. Finally, the authors' aim is to enhance the present methodology's robustness by including the fracture parameters of bulk adhesive, leading to a general study of the fracture initiation mechanism of the bonded joints.

Acknowledgement

The authors gratefully acknowledge Occitanie Region and Université Fédérale de Toulouse Midi-Pyrénées ISAE-SUPAERO for the financial support as well as the four reviewers for providing insightful contributions for the next developments. In addition, the authors want to gratefully thank Viviane Turq (Université de Toulouse, CIRIMAT) for her suggestions and helpful discussions about "small round" size. These works were performed in the frame of the scientific network TACCOS, meaning Toulouse Adhésion Cohésion Collage Structural (https://personnel.isae-supaero.fr/eric-paroissien/taccos-557.html, http://maelenn.aufray.free.fr/taccos.php).

Appendix A. Analysis of failure initiation and propagation

Previously described in Section 5.3, the post-mortem analyses were essential to help understand the interface debonding. First, the comportment of fracture initiation was indicated by the critical force *vs* critical surface response, as shown in Figure 23. In such a case, the classifications followed those defined in Section 3.1. The analysis showed a cohesive tendency (Fig. 6-c and 6-d), which corresponds to S_c *0*. On the other hand, as the critical force decreased, the small round surface started appearing. Finally, for low critical force, the identification of initiation and propagation becomes impossible.

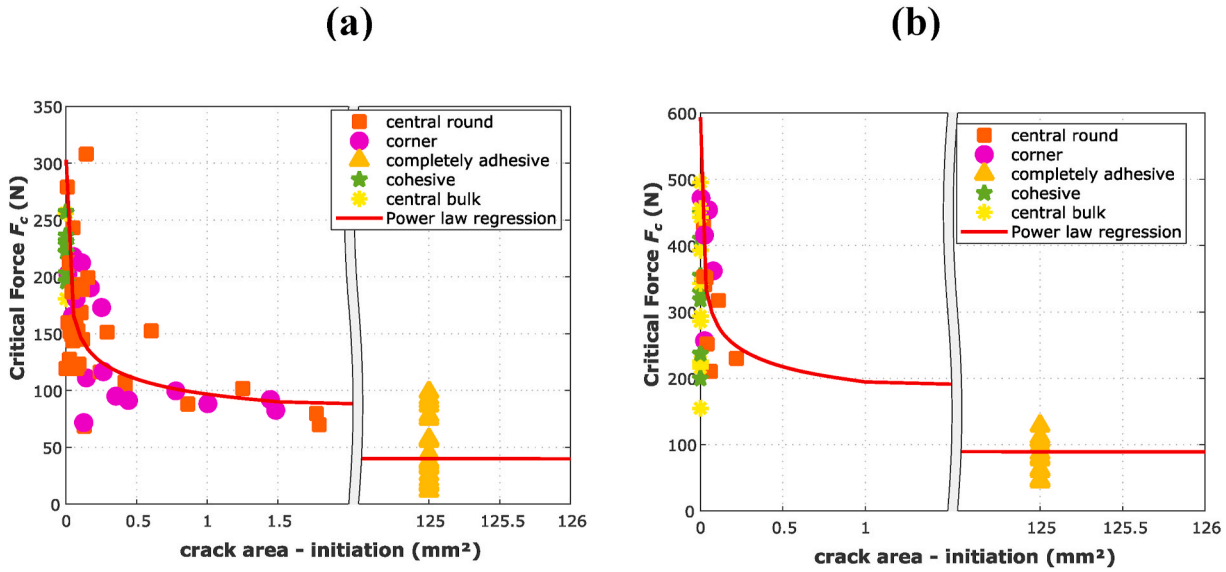

Fig. 23. Initiation behaviour in terms of critical load and critical surface at initiation (a) h_s=*1.08* mm and (b) h_s=*1.62* mm.

In this way, the general tendency of fracture initiation mechanism was related to the degree of interaction between the adhesive/substrate. A cohesive fracture initiation mechanism is expected for high adherence levels, whereas, for poor adherence, the failure initiation is indistinguishable from failure propagation.

In a similar procedure, each sample had its associate propagation comportment plotted (see Fig. 24) in terms of critical force, following the classification presented in Section 3.2. In special, high F_c implied an unstable behaviour. On the opposite side, for a low critical force, a more stable response was observed. Thus, the propagation behaviour is also associated with the ST: brittle propagation is generally expected for high adherence, whereas stable propagation for low adherence.

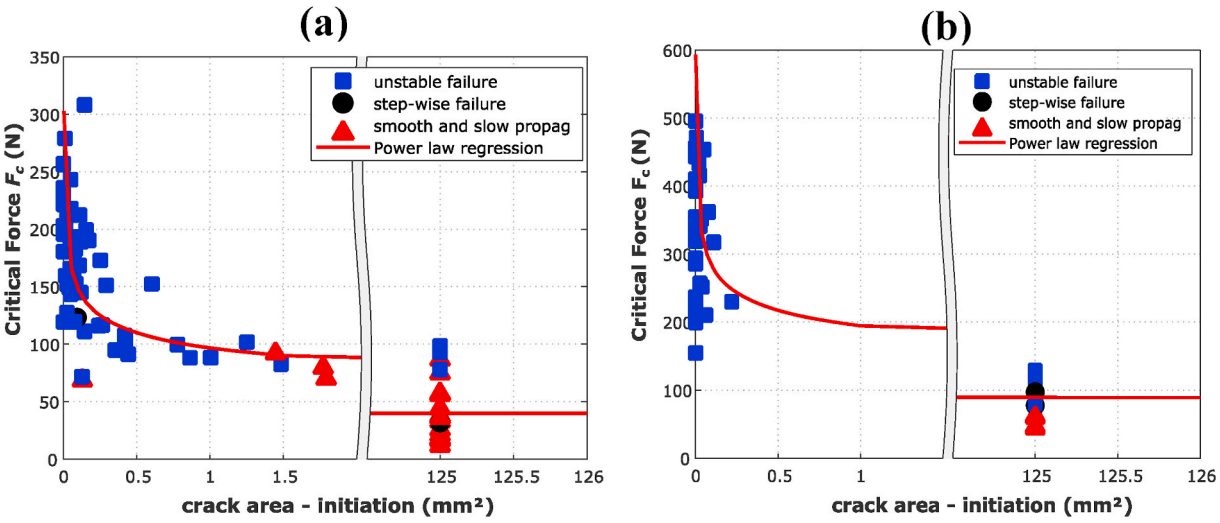

Fig. 24. Propagation behaviour in terms of the critical load and critical area at failure initiation (a) h_s=1.08 mm and (b) h_s=1.62 mm.

Finally, the post-mortem analyses established three threshold values, as follows:

- Cohesive-to-adhesive threshold: $S_c \sim 0.005$ mm^2
- Stability threshold: $S_c \sim 1.45$ mm^2
- adhesive threshold: $S_c \sim 1.8$ mm^2

Appendix B.1Robustness of ME technique: validation with FE model

As stated in Section 4.1, the ME technique has already been successfully used for the simplified stress analysis of bonded joints up to failure [15] as well as for the simulation of the delamination of composite laminates [16]. Thus, Appendix B.1 briefly demonstrates that the ME technique is suitable for modelling an adhesive block of 4 mm thick and 25 mm long as a beam.

A simplified and symmetric 3D FE model was created on SIEMENS-SAMCEF in order to compare with ME stress distribution along overlap length *(L)*. As shown in Fig. 25, two rigid rollers (radius 5 mm) were created, and a coefficient of friction of 0.1 was applied for both surface contact. Moreover, an x'-symmetry and z'-symmetry was imposed on all nodes in the plane y'z' and y'x', respectively.

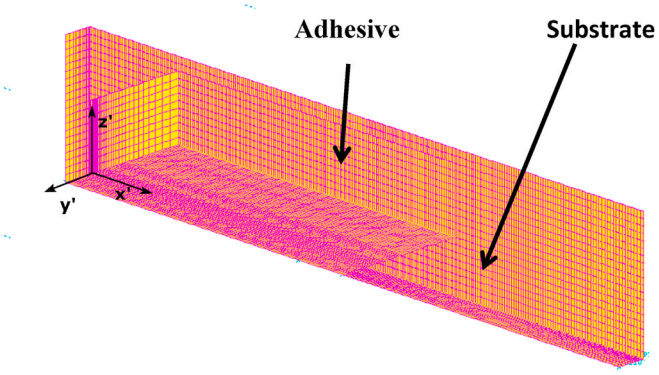

Fig. 25. 3D FE model developed on SIEMENS-SAMCEF.

The comparison was performed using a specific condition listed in Figs. 15 and 16, which wer also used by Birro et al. (2020) [14] and listed in Table 4.

Table 4
Experimental result of 3PBT – (Conditions: ST-III – Si:4 h–5% w/w – See Figs. 15 and 16).

Substrate thickness	F_c (N)	D_c (mm)	K_{spec} (N/mm)	S_c (mm^2)
1.08 mm	178 ± 26	0.61 ± 0.08	309 ± 9	0.102 ± 0.02

A 1D beam ME model was then configured using L_1 5.5 mm, k_I k_{II} 1710 N/mm, and a central displacement of the central roller D_c 0.58 mm. The overall stiffness of 3D FE model, 1D beam ME, and the experimental stiffnesses are traced in Fig. 26.

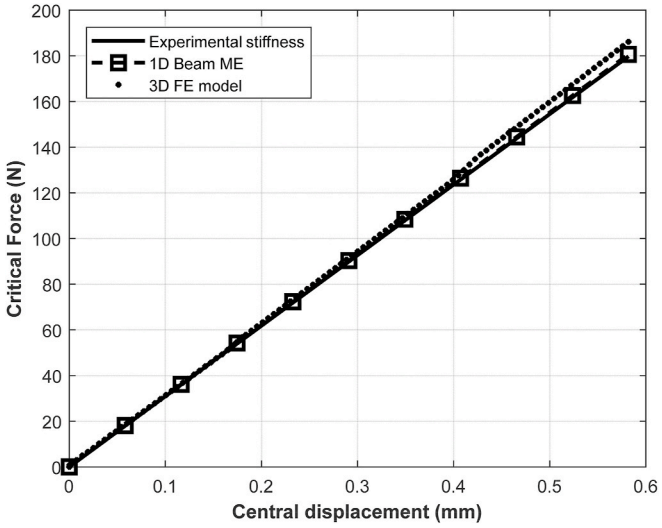

Fig. 26. Comparison of overall stiffness using ME technique and a 3D FE model.

Moreover, the 3D FE model has an important edges effect and stress concentration that are not considered in a 1D beam model. Moreover, the experimental samples possess a small filet radius (150 μm) in the corner, as discussed by Sauvage et al. (2019) [23]. Moreover, the ME model is a simplified model and does not consider corner's effect. Nonetheless, even though the ME model is a simplified model, a good agreement was obtained for the stress distribution along the overlap length (x' direction), as shown in Fig. 27.

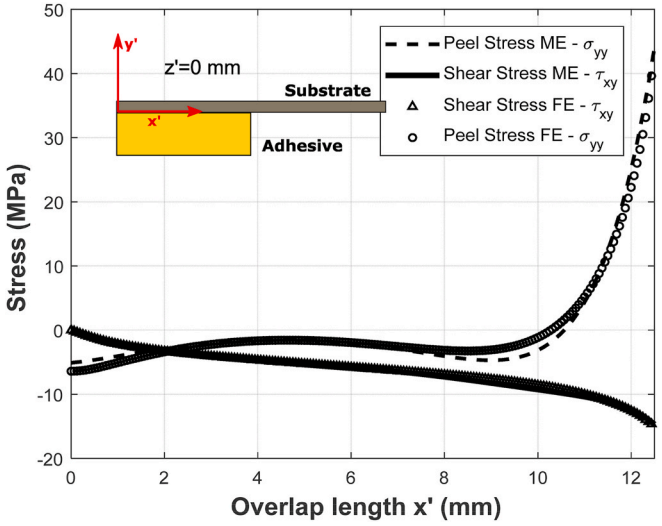

Fig. 27. Stress distribution along overlap length – A comparison between 1D Beam –ME and 3D FE models.

Moreover, the second interfacial shear stress τ_{xz} was computed along the width and shown in Fig. 28. Even though τ_{xz} could be incorporated into ME, the functionality is not included yet. On the other hand, Sauvage et al. (2019) [23] evaluated the stress state for crack initiation, and the conclusion was that fracture initiation is majority driven by peel stress. Thus, the stress distribution along the corner line (x' 12.5 mm, y' 0 and from z' 0 to z' 2.5 mm) was evaluated and demonstrated in Fig. 28, which confirmed that τ_{xz} had a minor influence on failure initiation.

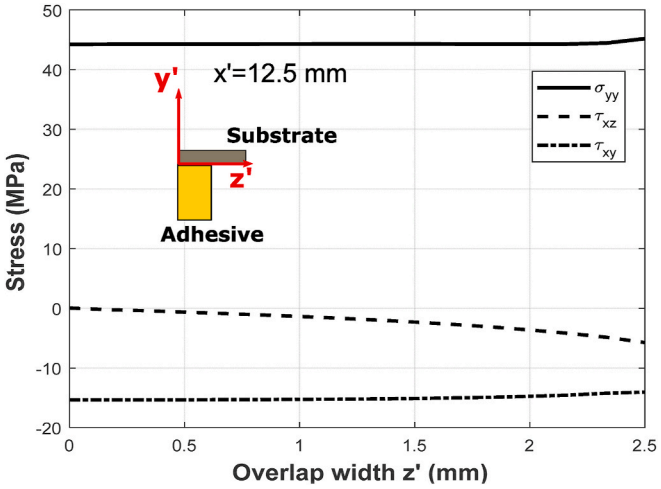

Fig. 28. Stress components τ_{xz} at the corner x' = 12.5 mm and y' = 0.

Appendix B.2Mode partition method using the Virtual Crack Closure Technique

The energy release rate can be assessed using different techniques, such as using the post-processed strain energy (available as an input in the ME method), J-integral and others. Carrere et al. (2015) [18] applied the Virtual Crack Closure Technique (VCCT) to determine $\mathcal{G}_{dif}$. Although VCCT not to be chosen in this paper to assess $\mathcal{G}_{dif}$, the technique is widely applied by commercial software, which includes SIEMENS-SAMCEF. Moreover, the method is useful for determining the mode I, II and III components of the differential energy release rate - $\mathcal{G}^{I}_{dif}$, $\mathcal{G}^{II}_{dif}$ and $\mathcal{G}^{III}_{dif}$, respectively. More details were provided by Carrere et al. (2015) [18].

Hence, the VCCT was applied to estimate each mode contribution using the 3D model presented in Appendix B.1. In special, a perfect bonding condition between substrate and adhesive is supposed (no cohesive elements), and different half crack lengths were analysed and listed in Table 5, as shown in Fig. 29. The boundary conditions and the coefficients of friction were previously listed in Appendix B.1.

Table 5
Case study of pre-cracked models for evaluating the differential energy release rate.

Case	$a_c/2$
1	0.5 mm
2	1.0 mm
3	1.5 mm
4	2.0 mm
5	2.5 mm

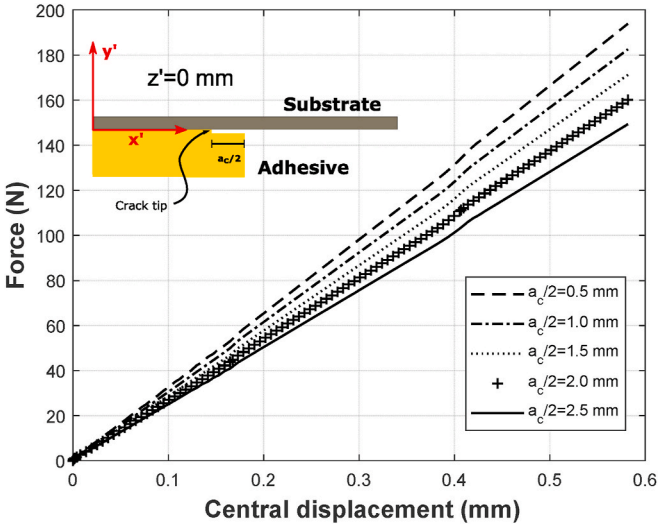

Fig. 29. Sketch of a pre-cracked model to determine mode partition using VCCT. The load versus central displacement of each model was also traced.

Finally, all energy release rates were computed for different crack length at the crack tip through the entire overlap width, from z' 0 to z' 2.5 mm (see Fig. 30). Thus, the analysis concluded also concluded that crack propagation is mainly driven by σ_{yy}.

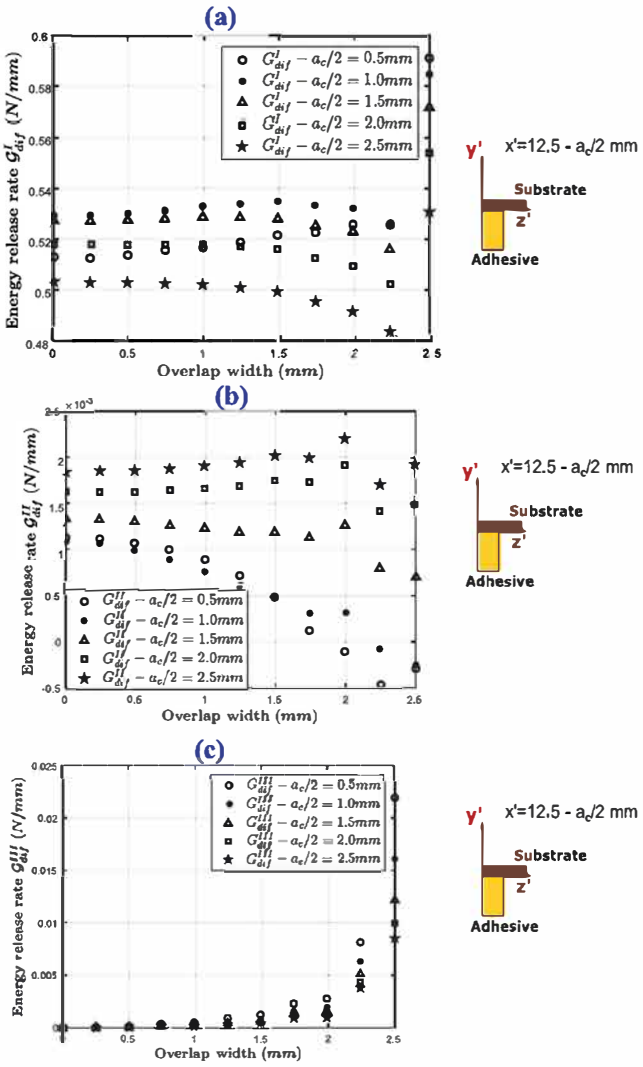

Fig. 30. Determination of mode I (a), mode II (b) and mode III (c) components of differential energy release rate via VCCT.

References

[1] Kumar S, Adams RD. Special issue on functionally graded adhesively bonded systems. Int J Adhesion Adhes 2017;76:1–2. https://doi.org/10.1016/j.ijadhadh.2017.05.002.

[2] Silva LFM, Ochsner A, Adams RD. Handbook of adhesion technology. second ed. Springer International Publishing; 2018. https://doi.org/10.1007/978-3-642-01169-6.

[3] Papon E. Adhesive families. In: Silva LFM, Ochsner A, Adams RD, editors. Handbook of adhesion technology. Springer International Publishing; 2011. p. 315–39. https://doi.org/10.1007/978-3-642-01169-6_14.

[4] Roche A, Gaillard F, Romand M, Fahnestock M. Metal-adhesive bonded systems: adhesion measurement using a three point flexure test. J Adhes Sci Technol 1987;1:145-57. https://doi.org/10.1163/156856187X00148.

[5] Legendre J, Créac'hcadec R, Gilbert F, Jacquet D. A new method to measure the adhesion capability of the metallic surface under shear loading using a modified Arcan test. J Adhes 2018;94:1017–35. https://doi.org/10.1080/00218464.2017.1334557.

[6] Zebar MEM, Hattali ML, Mesrati N. Interfacial fracture toughness measurement in both steady state and transient regimes using four-point bending test. Int J Fract 2020;222:123-35. https://doi.org/10.1007/s10704-020-00437-3.

[7] Roche A, Behme A, Solomon J. A three-point flexure test configuration for improved sensitivity to metal/adhesive interfacial phenomena. Int J Adhesion Adhes 1982;2:249–54. https://doi.org/10.1016/0143-7496(82)90032-X.

[8] ISO 14679. Adhesives – measurement of adhesion characteristics by a three-point bending method. Geneva, Switzerland: International Organization for Standardization; 1997.

[9] Sauvage JB, Aufray M, Jeandrau JP, Chalandon P, Poquillon D, Nardin M. Using the 3-point bending method to study failure initiation in epoxide-aluminium joints. Int J Adhesion Adhes 2017;75:181–9. https://doi.org/10.1016/j.ijadhadh.2017.03.011.

[10] Mittal KL. Adhesion measurement of thin films, thick films and bulk coating. West Conshohocken, PA: ASTM International; 1978. https://doi.org/10.1520/STP640-EB.

[11] Abel ML. Organosilanes: adhesion promoters and primers. In: Silva LFM, Ochsner A, Adams RD, editors. Handbook of adhesion technology. Springer International Publishing; 2011. p. 237–57. https://doi.org/10.1007/978-3-642-01169-6_11.

[12] Roche AA, Dole P, Bouzziri. Measurement of the practical adhesion of paint coatings to metallic sheets by the pull-off and the three point bending test. J Adhes Sci Technol 1994;8:587-609. https://doi.org/10.1163/156856194X00366.

[13] Watts JF. Surface characterisation and its rôle in adhesion science and technology. In: Silva LFM, Ochsner A, Adams RD, editors. Handbook of adhesion technology. Springer International Publishing; 2011. p. 179-207. https://doi.org/10.1007/978-3-642-01169-6_9.

[14] Birro TV, Paroissien E, Aufray M, Lachaud F. A methodology based on the coupled criterion for the assessment of adhesive-to-adherend interface crack initiation. Int J Adhesion Adhes 2020;102:102664. https://doi.org/10.1016/j.ijadhadh.2020.102664.

[15] Lelias G, Paroissien E, Lachaud F. Morlier J experimental characterization of cohesive zone models for thin adhesive layers loaded in mode I, mode II, and

mixed-mode I/II by the use of a direct method. Int J Solid Struct 2019;158:90–115. https://doi.org/10.1016/j.ijsolstr.2018.09.005.
[16] Lachaud F, Paroissien E, Michel L. Validation of a simplified analysis for the simulation of delamination of CFRP composite laminated materials under pure mode I. Compos Struct 2020;237:111897. https://doi.org/10.1016/j.compstruct.2020.111897.
[17] Leguillon D. Strength or toughness? A criterion for crack onset at a notch. Eur J Mech Solid 2002;21:61–72. https://doi.org/10.1016/S0997-7538(01)01184-6.
[18] Carrère N, Martin E, Leguillon D. Comparison between models based on a coupled criterion for the prediction of the failure of adhesively bonded joints. Eng Fract Mech 2015;138:185–201. https://doi.org/10.1016/j.engfracmech.2015.03.004.
[19] Martin E, Vandellos T, Leguillon D, Carrère N. Initiation of edge debonding: coupled criterion versus cohesive zone model. Int J Fract 2016;199:157–68. https://doi.org/10.1007/s10704-016-0101-2.
[20] Weißgraeber P, Becker W. Finite Fracture Mechanics model for mixed mode fracture in adhesive joints. Int J Solid Struct 2013;50:2383–94. https://doi.org/10.1016/j.ijsolstr.2013.03.012.
[21] Fraisse P, Schmit F. Use of J-integral as fracture parameter in simplified analysis of bonded joints. Int J Fract 1993;63:59–73. https://doi.org/10.1007/BF00053316.
[22] Aufray M, Roche AA. Epoxy–amine/metal interphases: influences from sharp needle-like crystal formation. Int J Adhesion Adhes 2007;27:387–93. https://doi.org/10.1016/j.ijadhadh.2006.09.009.
[23] Sauvage JB, Chalandon P, Poquillon D, Nardin M, Aufray M. Using the finite element analysis method to study the 3-point bending test for the characterisation of the adherence. Int J Appli Comput Mech 2020. https://doi.org/10.22055/JACM.2019.30337.1718. in press.